NANO LETTERS

pubs.acs.org/NanoLett

Letter

Superior Phonon-Limited Exciton Mobility in Lead-Free Two-Dimensional Perovskites

Linrui Jin, Carlos Mora Perez, Yao Gao, Ke Ma, Jee Yung Park, Shunran Li, Peijun Guo, Letian Dou, Oleg Prezhdo, and Libai Huang*

Cite This: *Nano Lett.* 2024, 24, 3638−3646

Read Online

ACCESS | Metrics & More | Article Recommendations | Supporting Information

ABSTRACT: Tin-based two-dimensional (2D) perovskites are emerging as lead-free alternatives in halide perovskite materials, yet their exciton dynamics and transport remain less understood due to defect scattering. Addressing this, we employed temperature-dependent transient photoluminescence (PL) microscopy to investigate intrinsic exciton transport in three structurally analogous Sn- and Pb-based 2D perovskites. Employing conjugated ligands, we synthesized high-quality crystals with enhanced phase stability at various temperatures. Our results revealed phonon-limited exciton transport in Sn perovskites, with diffusion constants increasing from 0.2 $cm^2\ s^{-1}$ at room temperature to 0.6 $cm^2\ s^{-1}$ at 40 K, and a narrowing PL line width. Notably, Sn-based perovskites exhibited greater exciton mobility than their Pb-based equivalents, which is attributed to lighter effective masses. Thermally activated optical phonon scattering was observed in Sn-based compounds but was absent in Pb-based materials. These findings, supported by molecular dynamics simulations, demonstrate that the phonon scattering mechanism in Sn-based halide perovskites can be distinct from their Pb counterparts.

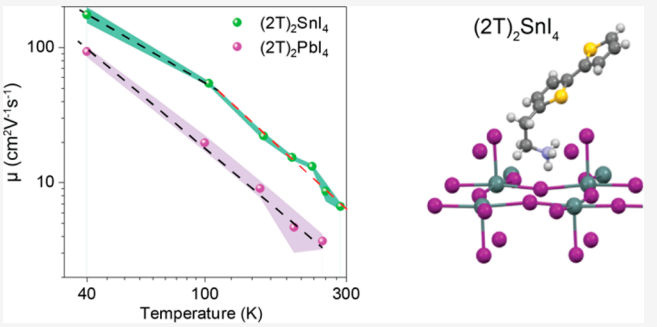

KEYWORDS: *2D materials, Exciton transport, Phonon scattering, Lead-free perovskites, Time-resolved microscopy*

Downloaded via UNIV OF SOUTHERN CALIFORNIA on April 14, 2025 at 22:51:22 (UTC).
See https://pubs.acs.org/sharingguidelines for options on how to legitimately share published articles.

Two-dimensional (2D) Ruddlesden−Popper (RP) phase metal halide perovskites have emerged as a new class of optoelectronic materials. Characterized by their strongly bound excitons and highly customizable structures, these materials have shown great promise in efficient light-emitting diodes and solar cells.[1−6] A critical factor in the performance of these optoelectronic devices is exciton diffusion. For instance, the capability to transport excitons over long distances is crucial to the efficiency of solar cells. There have been substantial research efforts in understanding exciton transport and phonon scattering in 2D Pb-based perovskites.[7−12] Specifically, long-chain organic ligands were found to play an important role in modulating electron−phonon scattering and exciton transport.[7−10] The transition from toxic Pb to alternative metals like environmentally friendlier Sn is desirable for many applications.[13−15] Solar cells and light-emitting diodes have been successfully fabricated from Sn-based quasi-2D and 2D perovskites.[16−22]

However, the performance of the Sn-based perovskites tends to lag behind Pb-based ones, largely due to deep defect levels that lead to carrier trapping.[13,23] Understanding the intrinsic role of organic and inorganic lattices in controlling exciton transport in low-defect materials is crucial for elucidating the link between the structure and device performance. Direct experimental investigations into exciton transport in Sn-based 2D perovskites are limited. The metal ion substitution from Pb to Sn can modify bond strength and give rise to different phonon modes.[9,24] On the other hand, the electronic structure can be modified in both the bandgap and the carrier effective mass. While theoretical calculations have predicted some favorable properties of the Sn-based materials, including light carrier effective masses and higher mobilities,[15,25,26] experimental validation of exciton transport in Sn-based 2D perovskites remains hampered by extrinsic defects.[27] To address these open questions, we conducted a direct comparison of exciton transport in three structurally analogous Sn- and Pb-based 2D perovskites, employing thiophene-based conjugated ligands[10,28] to achieve lower defect density. We observed that exciton diffusion constants increase as temperature decreases accompanied by narrower linewidths at low temperatures, suggesting that intrinsic phonon scatterings rather than defects limit exciton transport.

Received: December 13, 2023
Revised: March 6, 2024
Accepted: March 13, 2024
Published: March 18, 2024

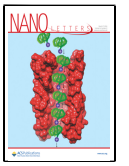

ACS Publications

© 2024 American Chemical Society

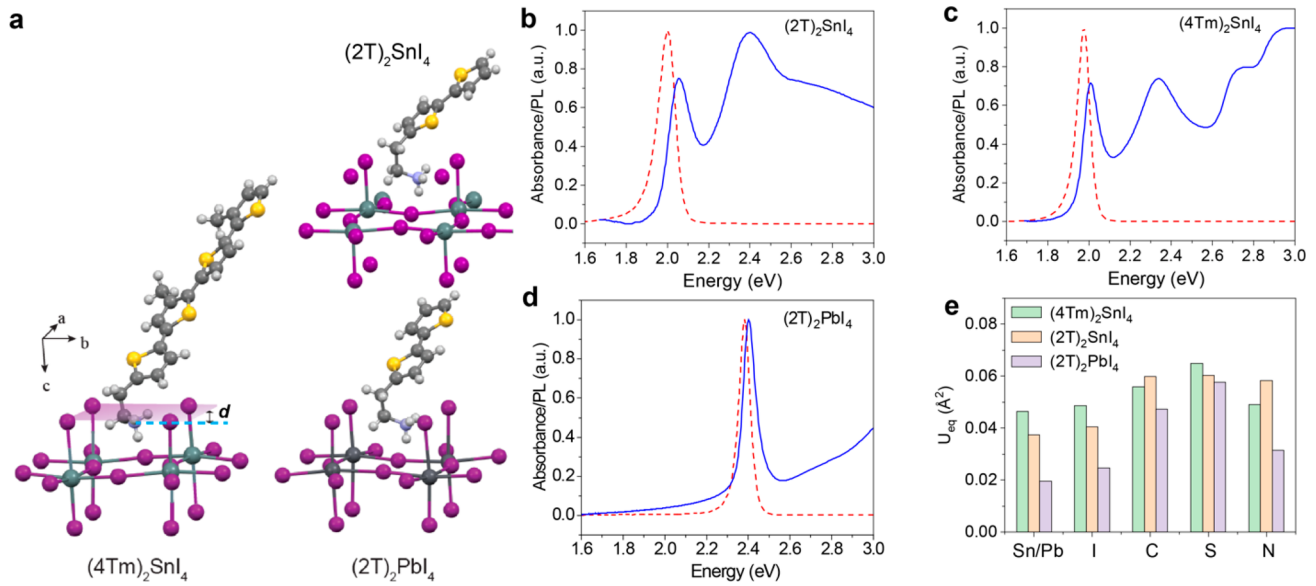

Figure 1. (a) Crystal structure illustration of $(4Tm)_2SnI_4$, $(2Tm)_2SnI_4$, and $(2T)_2PbI_4$. The ammonium-iodide plane distance *d* is depicted. (b–d) Room-temperature absorption (solid lines) and photoluminescence (dashed line) spectra, respectively. (e) Equilibrium atomic displacement of elements in $(4Tm)_2SnI_4$, $(2Tm)_2SnI_4$, and $(2T)_2PbI_4$.

STRUCTURE OF SN AND PB 2D PEROVSKITES WITH CONJUGATED LIGANDS

To access phonon-limited exciton transport, structure stability without a phase transition at low temperature is necessary. Taking advantage of the protection from the bulky long chain thiophene-based ligands, we selected $(4Tm)_2SnI_4$[29] and $(2T)_2SnI_4$[30] to study the photophysical properties of Sn-based 2D perovskite, for comparison with a structurally similar Pb-based counterpart $(2T)_2PbI_4$.[28] 4Tm is 2-(3″′,4′-dimethyl-[2,2′:5′,2″:5″,2″′-quaterthiophen]-5-yl) ethan-1-ammonium, and 2T is 2-([2,2′-bithiophen]-5-yl)ethan-1-ammonium. The crystal structures of the three samples are illustrated in Figure 1a. Figure S1 shows microscope images of representative $(4Tm)_2SnI_4$, $(2T)_2SnI_4$, and $(2T)_2PbI_4$ samples. All samples feature single crystalline domains exceeding a few micrometers in size, enabling the imaging of exciton diffusion within an individual domain. A type-I energy band alignment exists between $4Tm^+$, $2T^+$, and the inorganic lattice SnI_4^{2-} or PbI_4^{2-}, leading to excitons confined in the inorganic layers.[28] The optical response is dominated by excitons due to the reduced screening of the Coulombic interactions from the surrounding organic ligands.[31−35]

Sharp absorption and photoluminescence (PL) peaks originating from excitons were observed in all three structures, as depicted in Figure 1b–d. $(4Tm)_2SnI_4$ exhibits an exciton resonance at 630 nm (1.97 eV) and the PL emission is slightly higher in energy for $(2T)_2SnI_4$ due to the different structure and dielectric screening from the ligands. Compared to the Sn-based structures, $(2T)_2PbI_4$ has a larger bandgap and exciton resonance centers at 520 nm (2.39 eV). The primary PL emission peak aligns well with the strongest absorption feature at both room temperature and at 7 K (Figure S2), which supports the observed emission originating from the bright excitons. At room temperature, Stokes shifts of 33, 66, and 21 meV were observed for $(4Tm)_2SnI_4$, $(2T)_2SnI_4$, and $(2T)_2PbI_4$, respectively, and these values are similar to other reported values for 2D perovskites.[36] The Stokes shifts exhibit a correlation with the PL line widths, which can be attributed to anharmonic phonon scattering[37] and energetic disorder.[36] At 7 K, the Stokes shift significantly reduces, to only a few meV (Figure S2), due to predominantly harmonic phonon scattering at low temperatures.[37]

These thiophene-incorporated 2D perovskites show substantially smaller atomic displacement compared to aliphatic alkylammonium cations and overall more rigid lattices.[10] The corresponding single crystal X-ray diffraction (XRD) patterns (Figure S3) show a set of diffraction peaks confirming the formation of 2D RP perovskites for all three structures. Smaller Sn^{2+} results in a shorter metal–halide bond length and smaller lattice size in $(2T)_2SnI_4$ compared to $(2T)_2PbI_4$ (Table S1). As shown in Figure 1e, $(2T)_2PbI_4$ shows the least atomic displacement in both organic and inorganic components, consistent with its condensed packing.

EXCITON–PHONON SCATTERING

We performed temperature-dependent PL spectroscopy to investigate exciton transport and phonon scattering mechanisms. For all three structures, no phase transition was observed in the entire temperature range investigated. All three structures show narrowing of the PL line width as temperature decreases due to reduced phonon scattering.[38] At temperatures below 100 K, a lower-energy sideband was observed for the Sn-based structures, which was absent in the lead-based structure. This sideband exhibits a temperature-independent energy splitting of 37 and 48 meV for $(4Tm)_2SnI_4$ and $(2T)_2SnI_4$, respectively, as shown in Figure S4. These low-energy features were attributed to the optical phonon sideband, and the energy splittings are similar to previously reported values.[39] At 7 K, all three samples show a full width at half-maximum (fwhm) of around 10 meV. In an approximate model, the linewidth is the sum of inhomogeneous broadening due to scattering by disorder and imperfections in addition to the homogeneous broadening from radiative lifetime (Figure S5).[38,40] The observed exciton linewidths in this study are narrower when compared to those

https://doi.org/10.1021/acs.nanolett.3c04895
Nano Lett. 2024, 24, 3638−3646

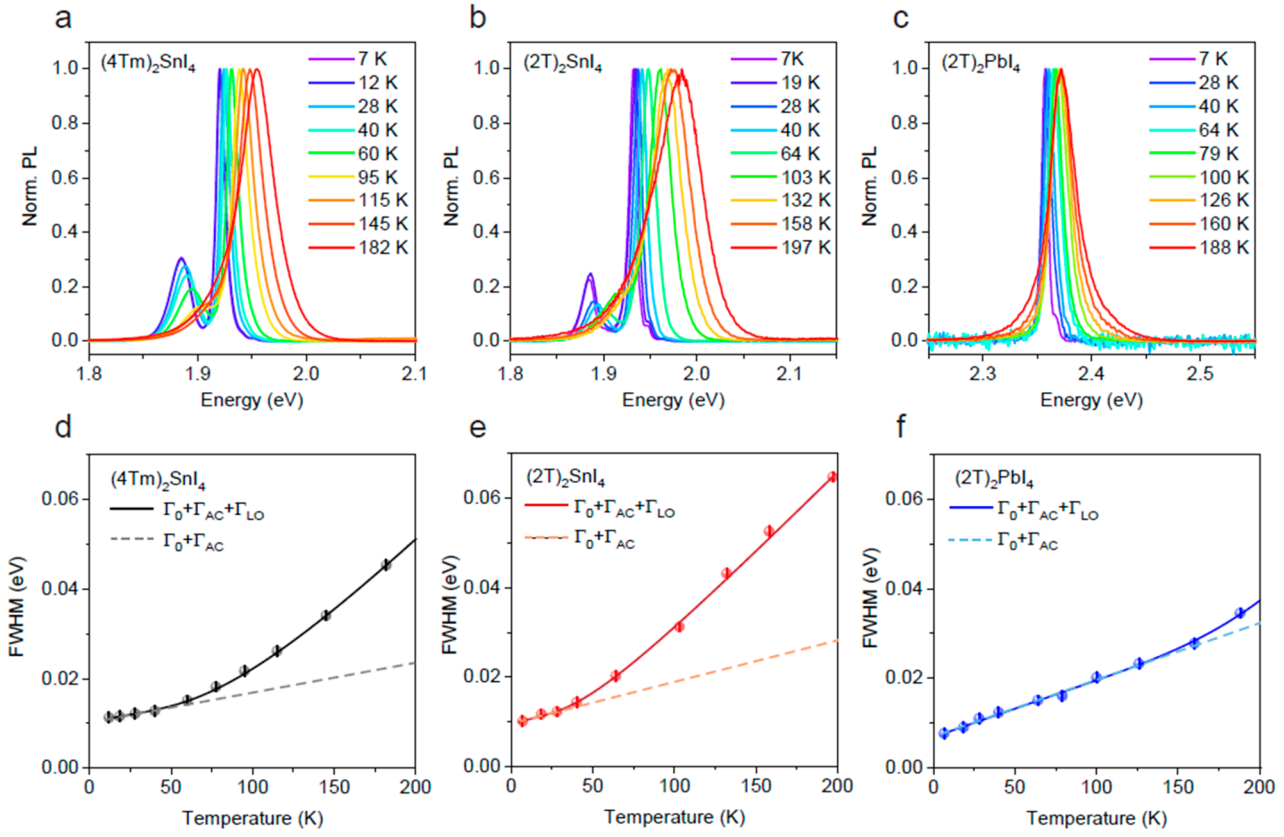

Figure 2. Temperature-dependent PL spectra of (a) $(4Tm)_2SnI_4$, (b) $(2T)_2SnI_4$, and (c) $(2T)_2PbI_4$. The full width at half-maximum (fwhm) extracted at each temperature is plotted in d and e, respectively. The solid lines are the fits to eq 1, involving different contributions from longitudinal the optical phonon (Γ_{LO}) and acoustic phonons (Γ_{ac}, dashed line) in addition to the zero-temperature line width (Γ_0).

Table 1. Fitting Parameters Used in Temperature-Dependent PL Linewidth

parameter	Γ_0 (eV)	Γ_{ac} (eV/K)	E_{LO} (eV)	Γ_{LO} (eV)
$(4Tm)_2SnI_4$	0.0104 ± 0.0004	$6.6 \times 10^{-5} \pm 1 \times 10^{-5}$	0.025 ± 0.003	0.09 ± 0.01
$(2T)_2SnI_4$	0.0096 ± 0.0005	$9 \times 10^{-5} \pm 2 \times 10^{-5}$	0.012 ± 0.002	0.039 ± 0.004
$(2T)_2PbI_4$	0.0069 ± 0.0002	$1.29 \times 10^{-4} \pm 4 \times 10^{-6}$		

observed in other Sn-based 2D perovskites.,[27,41] which suggests lower defect density.

Notably, a variation in the temperature dependence of the PL linewidth was observed. The emission linewidth for $(4Tm)_2SnI_4$ and $(2T)_2SnI_4$ displays a turning point in temperature, above which it broadens at an accelerated rate. This turning point corresponds to the onset of the nonlinear scattering of optical phonons that are strongly coupled to electronic states. The temperature-dependent occupation of these phonons follows the Bose−Einstein distribution.[40] In contrast, a linear dependence was observed for $(2T)_2PbI_4$. Lower-energy acoustic phonons or lower energy nonpolar optical phonons are activated at low temperatures, and the modulation to electronic states through deformation potential typically is assumed to have a linear temperature dependence.[40,42] The temperature dependent line width can be modeled approximately as[8,12,42−44]

$$\Gamma(T) = \Gamma_0 + \Gamma_{ac}T + \frac{\Gamma_{LO}}{\exp\left(\frac{E_{LO}}{k_B T}\right) - 1} \quad (1)$$

Γ_0 is the zero-temperature line width that include both homogeneous and inhomogeneous contribution, Γ_{ac} and Γ_{LO} are the coupling strength to acoustic phonon and longitudinal optical (LO) phonon scattering, respectively. Multiple optical phonon modes are likely to be coupled to the excitons, and E_{LO} is a representative energy for the weakly dispersive optical phonon branches.[42] In our simplified model, we assumed that the phonon coupling strengths Γ_{LO} and Γ_{AC} were temperature-independent. However, the dielectric response becomes more anharmonic and liquid-like at a higher temperature, resulting in phonon coupling strengths that indeed vary with temperature.[37] Due to this temperature dependence, we confined our model fitting to temperatures below 200 K to ensure accuracy. Data spanning the complete temperature spectrum are shown in Figure S6. The temperature-dependent linewidths of three samples were fitted using eq 1 with results shown in solid lines in Figure 2d,e. The fitting parameters are listed in Table 1.

These results imply that optical phonon scattering is the dominant mechanism for Sn-based structures, while lower energy phonon modes, such as acoustic phonons and possibly nonpolar optical phonons, play a more important role for Pb-based 2D perovskites with the same ligands. We note that a recent work on h-BN encapsulated $(PEA)_2PbI_4$ has shown strong coupling of excitons to optical phonons,[7] which suggests the role of organic ligand and the encapsulation in modulating

https://doi.org/10.1021/acs.nanolett.3c04895
Nano Lett. 2024, 24, 3638−3646

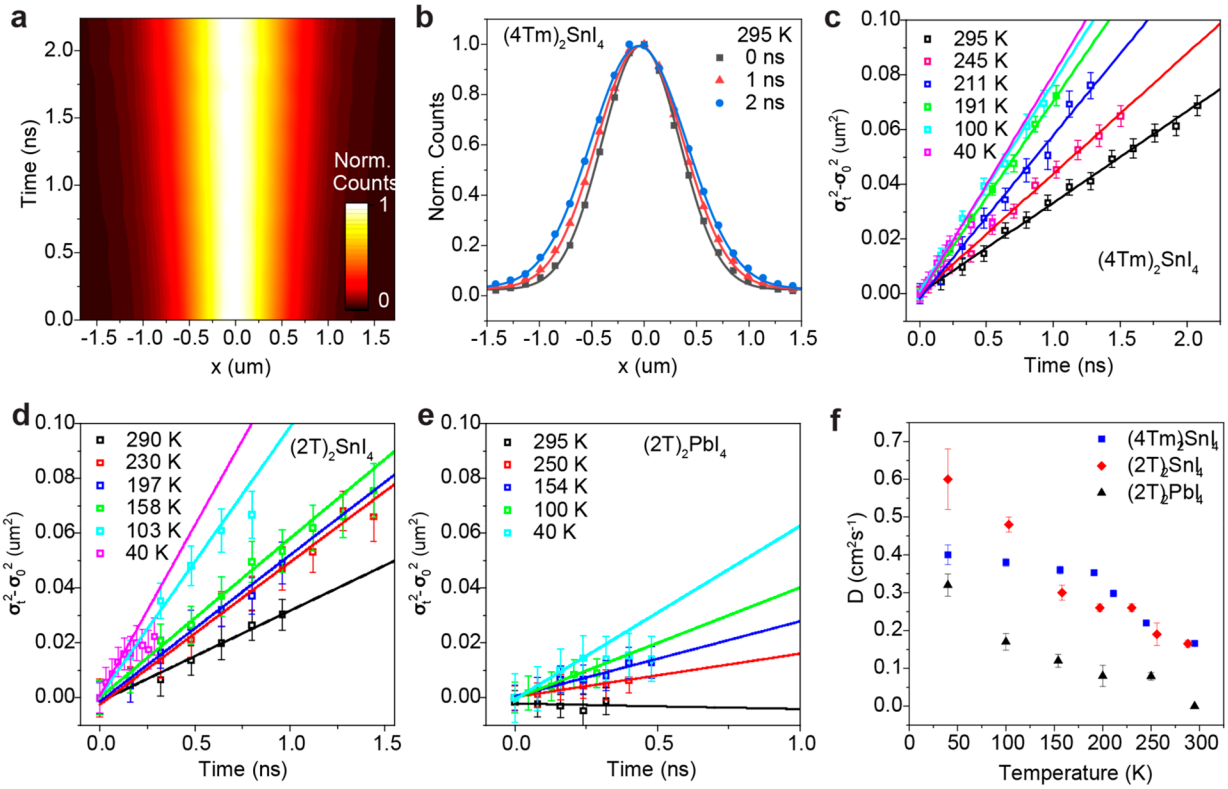

Figure 3. Temperature-dependent exciton transport of $(4Tm)_2SnI_4$, $(2Tm)_2SnI_4$, and $(2T)_2PbI_4$. (a) A representative time-resolved PL image of exciton diffusion in a crystalline domain of $(4Tm)_2SnI_4$ at room temperature. (b) The spatial profile at 0, 1, and 2 ns delay time extracted from panel a, with solid lines being the fits to a Gaussian function. (c–e) The squared variance change $(\sigma_t^2 - \sigma_0^2)$ extracted from spatial profiles at various temperatures. The solid lines are the fits to the data with linear equations to extract an exciton diffusion constant. $(4Tm)_2SnI_4$ (c), $(2T)_2SnI_4$ (d), and $(2T)_2PbI_4$ (e). (f) Temperature-dependent diffusivity of $(4Tm)_2SnI_4$, $(2Tm)_2SnI_4$, and $(2T)_2PbI_4$.

electron phonon scattering. Comparing $(4Tm)_2SnI_4$ and $(2T)_2SnI_4$, both Γ_{LO} and E_{LO} are higher in $(4Tm)_2SnI_4$. An E_{LO} of ~12 meV in $(2T)_2SnI_4$ matches the energy scale of the Sn–I stretching and bending mode. The smaller optical phonon energy in 2T-Sn compared to 4Tm–Sn (12 meV vs 25 meV) could be the result of the ammonium head of $(4Tm)_2SnI_4$ penetrating more into the inorganic lattice, as evidenced by the d value in Figure 1a. This could introduce higher energy modes such as torsion motion from the ammonium heads coupling to the electrons.[45] The bandgap of $4Tm^+$ being closer to SnI_4^{2-} also increases this possibility.[45] On the other hand, the C–H-p interactions between the 2T molecules is stronger compared to that of 4Tm molecules, which presents more steric hindrance to the motion of the NH_3 group and brings about a higher degree of rigidity.[45−47] A more rigid lattice would blue-shift the metal–halide vibrational modes.[24,39] This is indeed observed in the low-frequency Raman spectra (Figure S7) where the frequency of octahedral twisting, M–I–M bending, and M–I–M scissoring modes[39] of 2T-Sn are all blue-shifted.

PHONON-LIMITED EXCITON TRANSPORT

To investigate how different phonon scattering mechanisms impact transport, we imaged temperature-dependent exciton diffusion using transient PL microscopy[9,48−50] (see Methods in the SI and Figure S8 for details). Because of the large exciton binding energy of 2D perovskites, radiative recombination is a first-order process; i.e., PL intensity is proportional to exciton density. The temperature dependent PL lifetime and relative quantum yield (QY) are shown in Figure S5a–f. As the temperature decreases, the PL decay accelerates, and there is a corresponding increase in PL intensity and QY. This could be explained by a smaller exciton population distributed near momentum $k = 0$ at a higher temperature and therefore increases the radiative decay time and lowers QY.[51] Upon increasing the excitation density, no obvious change of decay traces was observed, which indicates that trapping or annihilation is not the limiting factor in the exciton dynamics.

The spatial and temporal dependence of the exciton population can be described by

$$\frac{\partial n(x, y, t)}{\partial t} = k_1 n(x, y, t) - D\nabla^2 n(x, y, t)$$

where k_1 is the exciton decay constant. Considering the nonunity PL quantum yield, k_1 includes processes of radiative recombination and trapping by nonluminescent states. The initial profile is dictated by the Gaussian excitation beam

$$n_0 = A_0 \exp\left(\frac{(x - x0)^2 + (y - y0)^2}{2\sigma_0^2}\right)$$

At time t,

$$n_t = A_t \exp\left(\frac{(x - x0)^2 + (y - y0)^2}{2\sigma_t^2}\right)$$

Considering the isotropic nature of the samples studied here, the 2D transport function in the ab plane of the crystal is reduced to 1D, and line scans were performed. An example of a plotted time-dependent exciton density map is shown in Figure

https://doi.org/10.1021/acs.nanolett.3c04895
Nano Lett. 2024, 24, 3638−3646

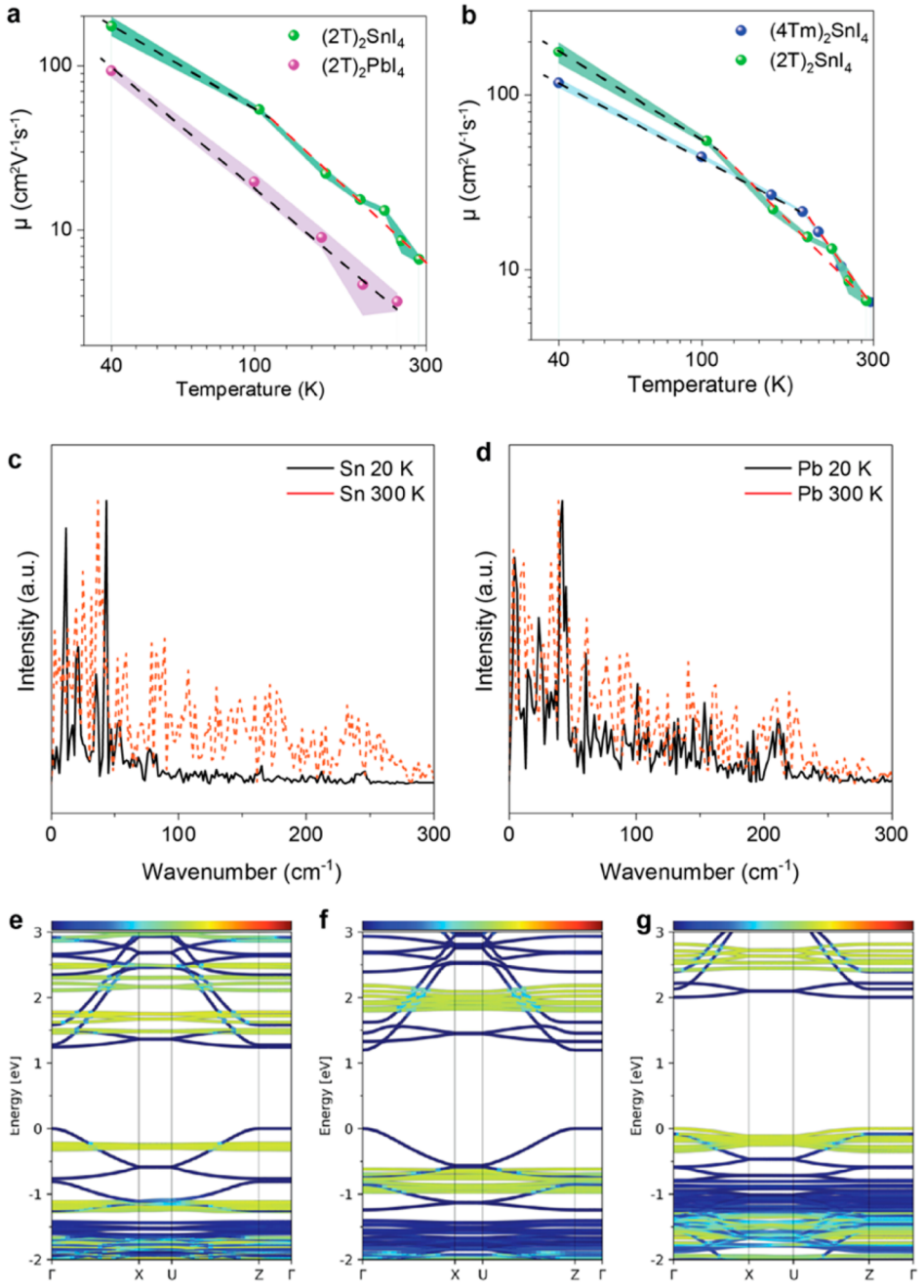

Figure 4. (a) Temperature-dependent mobility of $(2T)_2SnI_4$ and $(2T)_2PbI_4$ calculated from Figure 3f using the Einstein relation. The shaded area represents the experimental errors. Dashed lines are fitted with the power law dependence on temperature $T^{-\gamma}$. (b) Temperature-dependent mobility of $(4Tm)_2SnI_4$ plotted with that of $(2Tm)_2SnI_4$. The shaded area represents the experimental errors. Dashed lines are fitted with power law dependence on temperature $T^{-\gamma}$. (c,d) Temperature-dependent electron-vibrational influence spectra computed with *ab* initio molecular dynamics to identify vibrations that couple to the electronic subsystems in the Sn- and Pb-based 2D perovskites. (e–g) Electronic band structures of the $(4Tm)_2SnI_4$ (e), $(2T)_2SnI_4$ (f), and $(2T)_2PbI_4$ (g).

3a for $(4Tm)_2SnI_4$ measured at room temperature. By fitting the emission profile at each time delay with a Gaussian function (Figure 3b), we found a linear relationship between mean squared displacement $(\sigma_t^2 - \sigma_0^2)$ and time (t) with a diffusion constant (Figure 2c–e):

$$D = \frac{{\sigma_t}^2 - {\sigma_0}^2}{2t}$$

These results were obtained by averaging over multiple single-crystalline domains. All measurements were performed below an excitation density of ~200 nJ/cm^2, which corresponds to an exciton density around 10^{10} cm^{-2}, and exciton annihilation is negligible. (Figure S9).

As the temperature decreases, exciton diffusion accelerates in all three perovskites, which suggests that intrinsic phonon scattering is the primary factor influencing exciton transport. As temperature decreases, the population of phonons decreases, resulting in less frequent scattering of the excitons and thus higher diffusivity as well as a narrower emission linewidth.[38] In contrast, trap or defect limited transport would lead to the opposite temperature dependence, which was

https://doi.org/10.1021/acs.nanolett.3c04895
Nano Lett. 2024, 24, 3638–3646

reported for $(BA)_{2n}(MA)_{n-1}Pb_nI_{3n+1}$ (n = 2 and n = 4).[52] The temperature dependence observed resembles phonon-limited transport in conventional semiconductors and transition metal dichalcogenides (TMDCs).[53−55] At room temperature, a diffusivity of 0.17 ± 0.003 cm^2 s^{-1} was extracted for $(4Tm)_2SnI_4$, and a similar diffusivity was measured with $(2T)_2SnI_4$. For $(2T)_2PbI_4$, we were not able to reliably extract a diffusion constant at room temperature in the nanosecond time window due to the small range of motion of the excitons. At 40 K, D increases to 0.60 ± 0.08, 0.40 ± 0.03, and 0.32 ± 0.03 cm^2 $s^{-1}$for $(2T)_2SnI_4$, $(4Tm)_2SnI_4$, and $(2T)_2PbI_4$, respectively. The extracted diffusion constants of three samples are summarized in Figure 3f. The short lifetime observed at 40 K and lower temperatures (Figure S5) restricts the temporal window over which mean squared displacement (MSD) data can be collected. In addition, the decay kinetics at low temperatures diverge from a single exponential model, indicating the potential influence of other dark states at a long delay time. Our analysis concentrates on the initial linear phase of MSD expansion within the first nanosecond to extract the diffusion of the bright excitons.

The results from exciton-transport imaging experiments reveal that excitons in Sn-based 2D halide perovskites exhibit higher diffusivities compared with their Pb counterparts with the same ligands (Figure 3). Although excitons are neutral quasiparticles, their diffusivity can be correlated with charge mobility through the Einstein relation $\mu = D/(k_BT)$.[7] μ is as high as 100s of $cm^2 \cdot V^{-1} \cdot s^{-1}$ at low temperatures. The mobility values for these Sn-based 2D perovskites from our measuremnts are consistent with the values obtained from field-effect transistor devices (i.e., 2−9 $cm^2 \cdot V^{-1} \cdot s^{-1}$ at room temperature and increase at lower temperatures).[56] For all three structures, the mobility shows a power law dependence on temperature $T^{-\gamma}$(γ > 0, dashed lines in Figure 4a,b). This observation confirms phonon scattering being the main scattering source of excitons, because scattering by charge impurities or defects would lead to an opposite trend over temperature.[11]

The exponent γ differs between Sn- and Pb-based perovskites and depends on the organic ligands. For both $(4Tm)_2SnI_4$ and $(2T)_2SnI_4$, clearly two regimes of temperature dependence were observed (Figure 4b). γ is 1.0 ± 0.1 and 1.1 ± 0.1 for the low temperature regime (black dashed lines in Figure 4b) and 3.0 ± 0.1 and 2.6 ± 0.4 for the high temperature regime (red dashed lines), for $(4Tm)_2SnI_4$ and $(2T)_2SnI_4$, respectively. For 2D systems, $\gamma \sim 1$ indicates that acoustic phonons that require no thermal activation are the main scattering source.[11] The larger γ values at high temperatures reflect that both acoustic and thermally activated LO phonons play roles in scattering the excitons. The high-temperature results are consistent with a recent first-principles calculation of phonon scattering in $SiTiO_3$ showing a γ of 3 from the scattering by both LO and soft phonon modes at temperature higher than 150 K.[57] The turning point at ∼200 K for $(4Tm)_2SnI_4$ compared to the turning point at ∼100 K for $(2T)_2SnI_4$ agree with a higher representative LO phonon energy for $(4Tm)_2SnI_4$ (20 meV vs 12 meV) obtained from the line width fitting in Figure 2. In contrast, for $(2T)_2PbI_4$, the power law dependence shows very much one γ of 1.8 across the temperature range of 40 to 200 K. We note that the value of γ could also differ due the variations in band curvature and effective mass.[58]

FIRST-PRINCIPLES CALCULATIONS

We performed *ab initio* calculations using density functional theory (DFT) to elucidate the electron−phonon scattering mechanisms (Figures S10−S13), and further details are provided in the SI. To identify the crystal vibrations that couple to the electronic subsystem, we performed MD simulations. Perovskites are known to be highly anharmonic,[49] and MD simulations can capture anharmonicity explicitly. We reduced the computational cost by replacing the 2T or 4Tm ligands with Cs atoms (Figure S11). The Fourier transforms of autocorrelation functions of vibrational fluctuations of the electronic bandgaps were calculated, which gives electron-vibrational influence spectra identifying the phonon modes that couple to the electronic subsystem (Figure 4c,d). As shown in Figure 4c, the high-frequency exciton scattering in Sn-based perovskites is thermally activated and much more substantial at 300 K compared to 20 K. In contrast, the temperature dependence is much weaker for Pb (Figure 4d), where the spectra are similar for 20 and 300 K, consistent with the lower thermal activation. This difference in thermal activation of phonons for Sn and Pb is in great agreement with the temperature dependence of PL line width and exciton diffusivity (Figure 2 and Figure 4c,d).

Finally, we also calculate the band structure (Figure 4e−g and Figure S12) and projected density of states (Figure S13) for all three structures including organic ligands to obtain electron and hole effective masses. The conduction band minimum (CBM) does not contain any organic ligand contributions in all structures but is solely composed of the perovskite core, with a larger contribution from the metal (Sn/Pb). $(2T)_2SnI_4$ possesses the lightest effective electron mass (m_e^* = 0.0868 m_e) of all three systems studied here (Figure S12). The valence band maximum (VBM) of the Sn-based systems originates entirely from the perovskite core (Sn−I), with a slightly more significant contribution from the halide. The organic ligand states are located deeper within the VB for the 2T compared to the 4Tm ligands. The hole effective mass for $(4Tm)_2SnI_4$ (m_h^* = −0.1470 m_e) is similar to that in $(2T)_2SnI_4$ (m_h^* = −0.1413 m_e). Overall, $(2T)_2PbI_4$ has the largest effective mass values for both the electron and hole, which explains the lowest exciton mobility. The electron and hole effective masses are listed in Table S2. The combined MD simulations with band structure calculations provide a microscopic understanding of the temperature-dependent PL linewidth and exciton transport behavior. The relatively light effective mass of $(2T)_2SnI_4$ aligns with its enhanced exciton mobility at lower temperatures. Exciton scattering by high-energy phonon modes in Sn-based compounds at high temperatures is consistent with the temperature-dependent changes in PL linewidth and exciton diffusivity measurements. In contrast, the phonon modes in $(2T)_2PbI_4$ are already active at low temperatures.

CONCLUSIONS

We investigated the fundamental phonon scattering mechanisms that dictate exciton transport in both Sn- and Pb-based 2D perovskites. The stronger intermolecular interaction between π-conjugated ligands facilitates a more rigid inorganic crystal lattice, which allows for the investigation of intrinsic phonon-limited exciton transport. These results demonstrate that excitons in Sn-based halide perovskites are intrinsically mobile, with mobility as high as 100 cm^2 V^{-1} s^{-1} at 40 K. More

https://doi.org/10.1021/acs.nanolett.3c04895
Nano Lett. 2024, 24, 3638−3646

crucially, Sn-based perovskites exhibit, in certain aspects, superior transport properties compared to the Pb counterparts, ascribed to their lighter effective mass. Phonon scattering mechanisms are also notably different, with nonlinear onset of optical phonon scattering observed Sn but absent for Pb. The incorporation of organic conjugated ligands opens avenues for modulating phonon coupling to optoelectronic application needs and presents an opportunity to explore approaches to enhance performance while maintaining environmental sustainability.

■ ASSOCIATED CONTENT

Supporting Information

The Supporting Information is available free of charge at https://pubs.acs.org/doi/10.1021/acs.nanolett.3c04895.

Methods, sample characterization, MD and band structure calculations, supplemental figures and tables (PDF)

■ AUTHOR INFORMATION

Corresponding Author

Libai Huang − *Department of Chemistry, Purdue University, West Lafayette, Indiana 47907, United States;* orcid.org/0000-0001-9975-3624; Email: libai-huang@purdue.edu

Authors

Linrui Jin − *Department of Chemistry, Purdue University, West Lafayette, Indiana 47907, United States;* orcid.org/0000-0002-1416-786X

Carlos Mora Perez − *Departments of Chemistry and Physics and Astronomy, University of Southern California, Los Angeles, California 90007, United States;* orcid.org/0000-0001-8840-5093

Yao Gao − *Davidson School of Chemical Engineering, Purdue University, West Lafayette, Indiana 47907, United States*

Ke Ma − *Davidson School of Chemical Engineering, Purdue University, West Lafayette, Indiana 47907, United States*

Jee Yung Park − *Davidson School of Chemical Engineering, Purdue University, West Lafayette, Indiana 47907, United States;* orcid.org/0000-0002-9814-6563

Shunran Li − *Department of Chemical and Environmental Engineering, Yale University, New Haven, Connecticut 06520, United States; Energy Sciences Institute, Yale University, West Haven, Connecticut 06516, United States;* orcid.org/0000-0003-0428-295X

Peijun Guo − *Department of Chemical and Environmental Engineering, Yale University, New Haven, Connecticut 06520, United States; Energy Sciences Institute, Yale University, West Haven, Connecticut 06516, United States;* orcid.org/0000-0001-5732-7061

Letian Dou − *Department of Chemistry, Purdue University, West Lafayette, Indiana 47907, United States; Davidson School of Chemical Engineering and Birck Nanotechnology Center, Purdue University, West Lafayette, Indiana 47907, United States;* orcid.org/0000-0001-6411-8591

Oleg Prezhdo − *Departments of Chemistry and Physics and Astronomy, University of Southern California, Los Angeles, California 90007, United States;* orcid.org/0000-0002-5140-7500

Complete contact information is available at: https://pubs.acs.org/10.1021/acs.nanolett.3c04895

Notes

The authors declare no competing financial interest.

■ ACKNOWLEDGMENTS

The optical characterization, sample synthesis and preparation effort at Purdue was supported by U.S. Department of Energy, Office of Basic Energy Sciences through award DE-SC0022082. The computational work at the University of Southern California was supported by the U.S. National Science Foundation grant CHE-2154367.

■ REFERENCES

(1) Dou, L.; Wong, A. B.; Yu, Y.; Lai, M.; Kornienko, N.; Eaton, S. W.; Fu, A.; Bischak, C. G.; Ma, J.; Ding, T.; Ginsberg, N. S.; Wang, L.-W.; Alivisatos, A. P.; Yang, P. Atomically thin two-dimensional organic-inorganic hybrid perovskites. *Science* **2015**, *349*, 1518−1521.

(2) Tsai, H.; Nie, W.; Blancon, J.-C.; Stoumpos, C. C.; Asadpour, R.; Harutyunyan, B.; Neukirch, A. J.; Verduzco, R.; Crochet, J. J.; Tretiak, S.; Pedesseau, L.; Even, J.; Alam, M. A.; Gupta, G.; Lou, J.; Ajayan, P. M.; Bedzyk, M. J.; Kanatzidis, M. G.; Mohite, A. D. High-efficiency two-dimensional Ruddlesden−Popper perovskite solar cells. *Nature* **2016**, *536*, 312−316.

(3) Grancini, G.; Roldan-Carmona, C.; Zimmermann, I.; Mosconi, E.; Lee, X.; Martineau, D.; Narbey, S.; Oswald, F.; De Angelis, F.; Graetzel, M.; Nazeeruddin, M. K. One-Year stable perovskite solar cells by 2D/3D interface engineering. *Nat. Commun.* **2017**, *8*, 1−8.

(4) Lee, J.-W.; Dai, Z.; Han, T.-H.; Choi, C.; Chang, S.-Y.; Lee, S.-J.; De Marco, N.; Zhao, H.; Sun, P.; Huang, Y.; Yang, Y. 2D perovskite stabilized phase-pure formamidinium perovskite solar cells. *Nat. Commun.* **2018**, *9*, 1−10.

(5) Liu, Y.; Akin, S.; Pan, L.; Uchida, R.; Arora, N.; Milić, J. V.; Hinderhofer, A.; Schreiber, F.; Uhl, A. R.; Zakeeruddin, S. M.; Hagfeldt, A.; Dar, M. I.; Grätzel, M. Ultrahydrophobic 3D/2D fluoroarene bilayer-based water-resistant perovskite solar cells with efficiencies exceeding 22%. *Science Advances* **2019**, *5*, No. eaaw2543.

(6) Wang, N.; Cheng, L.; Ge, R.; Zhang, S.; Miao, Y.; Zou, W.; Yi, C.; Sun, Y.; Cao, Y.; Yang, R.; Wei, Y.; Guo, Q.; Ke, Y.; Yu, M.; Jin, Y.; Liu, Y.; Ding, Q.; Di, D.; Yang, L.; Xing, G.; Tian, H.; Jin, C.; Gao, F.; Friend, R. H.; Wang, J.; Huang, W. Perovskite light-emitting diodes based on solution-processed self-organized multiple quantum wells. *Nat. Photonics* **2016**, *10*, 699−704.

(7) Ziegler, J. D.; Zipfel, J.; Meisinger, B.; Menahem, M.; Zhu, X.; Taniguchi, T.; Watanabe, K.; Yaffe, O.; Egger, D. A.; Chernikov, A. Fast and Anomalous Exciton Diffusion in Two-Dimensional Hybrid Perovskites. *Nano Lett.* **2020**, *20*, 6674−6681.

(8) Gong, X.; Voznyy, O.; Jain, A.; Liu, W.; Sabatini, R.; Piontkowski, Z.; Walters, G.; Bappi, G.; Nokhrin, S.; Bushuyev, O.; Yuan, M.; Comin, R.; McCamant, D.; Kelley, S. O.; Sargent, E. H. Electron-phonon interaction in efficient perovskite blue emitters. *Nat. Mater.* **2018**, *17*, 550−556.

(9) Seitz, M.; Magdaleno, A. J.; Alcazar-Cano, N.; Melendez, M.; Lubbers, T. J.; Walraven, S. W.; Pakdel, S.; Prada, E.; Delgado-Buscalioni, R.; Prins, F. Exciton diffusion in two-dimensional metal-halide perovskites. *Nat. Commun.* **2020**, *11*, 2035.

(10) Park, J. Y.; Song, R.; Liang, J.; Jin, L.; Wang, K.; Li, S.; Shi, E.; Gao, Y.; Zeller, M.; Teat, S. J.; Guo, P.; Huang, L.; Zhao, Y. S.; Blum, V.; Dou, L. Thickness control of organic semiconductor-incorporated perovskites. *Nat. Chem.* **2023**, *15*, 1745−1753.

(11) Guo, Z.; Wu, X.; Zhu, T.; Zhu, X.; Huang, L. Electron−Phonon Scattering in Atomically Thin 2D Perovskites. *ACS Nano* **2016**, *10*, 9992−9998.

(12) Ni, L.; Huynh, U.; Cheminal, A.; Thomas, T. H.; Shivanna, R.; Hinrichsen, T. F.; Ahmad, S.; Sadhanala, A.; Rao, A. Real-Time Observation of Exciton-Phonon Coupling Dynamics in Self-Assembled Hybrid Perovskite Quantum Wells. *ACS Nano* **2017**, *11*, 10834−10843.

(13) Ke, W.; Kanatzidis, M. G. Prospects for low-toxicity lead-free perovskite solar cells. *Nat. Commun.* **2019**, *10*, 965.

(14) Giustino, F.; Snaith, H. J. Toward Lead-Free Perovskite Solar Cells. *ACS Energy Letters* **2016**, *1*, 1233−1240.
(15) Wang, Z.; Ganose, A. M.; Niu, C.; Scanlon, D. O. First-principles insights into tin-based two-dimensional hybrid halide perovskites for photovoltaics. *Journal of Materials Chemistry A* **2018**, *6*, 5652−5660.
(16) Cao, D. H.; Stoumpos, C. C.; Yokoyama, T.; Logsdon, J. L.; Song, T.-B.; Farha, O. K.; Wasielewski, M. R.; Hupp, J. T.; Kanatzidis, M. G. Thin Films and Solar Cells Based on Semiconducting Two-Dimensional Ruddlesden−Popper (CH3(CH2)3NH3)2(CH3NH3)-n−1SnnI3n+1 Perovskites. *ACS Energy Letters* **2017**, *2*, 982−990.
(17) Lanzetta, L.; Marin-Beloqui, J. M.; Sanchez-Molina, I.; Ding, D.; Haque, S. A. Two-Dimensional Organic Tin Halide Perovskites with Tunable Visible Emission and Their Use in Light-Emitting Devices. *ACS Energy Letters* **2017**, *2*, 1662−1668.
(18) Wang, K.; Jin, L.; Gao, Y.; Liang, A.; Finkenauer, B. P.; Zhao, W.; Wei, Z.; Zhu, C.; Guo, T.-F.; Huang, L.; Dou, L. Lead-Free Organic−Perovskite Hybrid Quantum Wells for Highly Stable Light-Emitting Diodes. *ACS Nano* **2021**, *15*, 6316−6325.
(19) Guan, J.; Sagar, L. K.; Li, R.; Wang, D.; Bappi, G.; Watkins, N. E.; Bourgeois, M. R.; Levina, L.; Fan, F.; Hoogland, S.; Voznyy, O.; Martins de Pina, J.; Schaller, R. D.; Schatz, G. C.; Sargent, E. H.; Odom, T. W. Engineering Directionality in Quantum Dot Shell Lasing Using Plasmonic Lattices. *Nano Lett.* **2020**, *20*, 1468−1474.
(20) Yuan, F.; Zheng, X.; Johnston, A.; Wang, Y.-K.; Zhou, C.; Dong, Y.; Chen, B.; Chen, H.; Fan, J. Z.; Sharma, G.; Li, P.; Gao, Y.; Voznyy, O.; Kung, H.-T.; Lu, Z.-H.; Bakr, O. M.; Sargent, E. H. Color-pure red light-emitting diodes based on two-dimensional lead-free perovskites. *Science Advances* **2020**, *6*, No. eabb0253.
(21) Tong, J.; Jiang, Q.; Ferguson, A. J.; Palmstrom, A. F.; Wang, X.; Hao, J.; Dunfield, S. P.; Louks, A. E.; Harvey, S. P.; Li, C.; Lu, H.; France, R. M.; Johnson, S. A.; Zhang, F.; Yang, M.; Geisz, J. F.; McGehee, M. D.; Beard, M. C.; Yan, Y.; Kuciauskas, D.; Berry, J. J.; Zhu, K. Carrier control in Sn−Pb perovskites via 2D cation engineering for all-perovskite tandem solar cells with improved efficiency and stability. *Nature Energy* **2022**, *7*, 642−651.
(22) Guo, Y.; Sun, M.; Yang, W.; Yuan, S.; Xiong, H.; Tan, Z.; Fan, J.; Li, W. Enhanced Charge Transport by Regulating the Electronic Structure in 2D Tin-Based Perovskite Solar Cells. *J. Phys. Chem. C* **2022**, *126*, 9425−9436.
(23) Wang, J.; Su, R.; Xing, J.; Bao, D.; Diederichs, C.; Liu, S.; Liew, T. C. H.; Chen, Z.; Xiong, Q. Room Temperature Coherently Coupled Exciton-Polaritons in Two-Dimensional Organic-Inorganic Perovskite. *ACS Nano* **2018**, *12*, 8382−8389.
(24) Fu, J.; Li, M.; Solanki, A.; Xu, Q.; Lekina, Y.; Ramesh, S.; Shen, Z. X.; Sum, T. C. Electronic States Modulation by Coherent Optical Phonons in 2D Halide Perovskites. *Adv. Mater.* **2021**, *33*, No. e2006233.
(25) Poncé, S.; Schlipf, M.; Giustino, F. Origin of Low Carrier Mobilities in Halide Perovskites. *ACS Energy Letters* **2019**, *4*, 456−463.
(26) Wang, K.; Liang, Z.; Wang, X.; Cui, X. Lead Replacement in CH3NH3PbI3Perovskites. *Advanced Electronic Materials* **2015**, *1*, No. 1500089.
(27) Zhang, T.; Zhou, C.; Feng, X.; Dong, N.; Chen, H.; Chen, X.; Zhang, L.; Lin, J.; Wang, J. Regulation of the luminescence mechanism of two-dimensional tin halide perovskites. *Nat. Commun.* **2022**, *13*, 60.
(28) Gao, Y.; Shi, E.; Deng, S.; Shiring, S. B.; Snaider, J. M.; Liang, C.; Yuan, B.; Song, R.; Janke, S. M.; Liebman-Pelaez, A.; Yoo, P.; Zeller, M.; Boudouris, B. W.; Liao, P.; Zhu, C.; Blum, V.; Yu, Y.; Savoie, B. M.; Huang, L.; Dou, L. Molecular engineering of organic-inorganic hybrid perovskites quantum wells. *Nat. Chem.* **2019**, *11*, 1151−1157.
(29) Gao, Y.; Wei, Z.; Yoo, P.; Shi, E.; Zeller, M.; Zhu, C.; Liao, P.; Dou, L. Highly Stable Lead-Free Perovskite Field-Effect Transistors Incorporating Linear pi-Conjugated Organic Ligands. *J. Am. Chem. Soc.* **2019**, *141*, 15577−15585.
(30) Ma, K.; Hsu, S.-N.; Gao, Y.; Wei, Z.; Jin, L.; Finkenauer, B. P.; Huang, L.; Boudouris, B. W.; Mei, J.; Dou, L. Organic Cation Engineering for Vertical Charge Transport in Lead-Free Perovskite Quantum Wells. *Small Science* **2021**, *1*, No. 2000024.
(31) Yaffe, O.; Chernikov, A.; Norman, Z. M.; Zhong, Y.; Velauthapillai, A.; van der Zande, A.; Owen, J. S.; Heinz, T. F. Excitons in ultrathin organic-inorganic perovskite crystals. *Phys. Rev. B* **2015**, *92*, No. 045414.
(32) Blancon, J. C.; Stier, A. V.; Tsai, H.; Nie, W.; Stoumpos, C. C.; Traore, B.; Pedesseau, L.; Kepenekian, M.; Katsutani, F.; Noe, G. T.; Kono, J.; Tretiak, S.; Crooker, S. A.; Katan, C.; Kanatzidis, M. G.; Crochet, J. J.; Even, J.; Mohite, A. D. Scaling law for excitons in 2D perovskite quantum wells. *Nat. Commun.* **2018**, *9*, 2254.
(33) Mauck, C. M.; Tisdale, W. A. Excitons in 2D Organic−Inorganic Halide Perovskites. *Trends in Chemistry* **2019**, *1*, 380−393.
(34) Katan, C.; Mercier, N.; Even, J. Quantum and Dielectric Confinement Effects in Lower-Dimensional Hybrid Perovskite Semiconductors. *Chem. Rev.* **2019**, *119*, 3140−3192.
(35) Filip, M. R.; Qiu, D. Y.; Del Ben, M.; Neaton, J. B. Screening of Excitons by Organic Cations in Quasi-Two-Dimensional Organic−Inorganic Lead-Halide Perovskites. *Nano Lett.* **2022**, *22*, 4870−4878.
(36) Straus, D. B.; Iotov, N.; Gau, M. R.; Zhao, Q.; Carroll, P. J.; Kagan, C. R. Longer Cations Increase Energetic Disorder in Excitonic 2D Hybrid Perovskites. *J. Phys. Chem. Lett.* **2019**, *10*, 1198−1205.
(37) Guo, Y.; Yaffe, O.; Hull, T. D.; Owen, J. S.; Reichman, D. R.; Brus, L. E. Dynamic emission Stokes shift and liquid-like dielectric solvation of band edge carriers in lead-halide perovskites. *Nat. Commun.* **2019**, *10*, 1175.
(38) Feldstein, D.; Perea-Causín, R.; Wang, S.; Dyksik, M.; Watanabe, K.; Taniguchi, T.; Plochocka, P.; Malic, E. Microscopic Picture of Electron−Phonon Interaction in Two-Dimensional Halide Perovskites. *J. Phys. Chem. Lett.* **2020**, *11*, 9975−9982.
(39) Thouin, F.; Valverde-Chavez, D. A.; Quarti, C.; Cortecchia, D.; Bargigia, I.; Beljonne, D.; Petrozza, A.; Silva, C.; Srimath Kandada, A. R. Phonon coherences reveal the polaronic character of excitons in two-dimensional lead halide perovskites. *Nat. Mater.* **2019**, *18*, 349−356.
(40) Rudin, S.; Reinecke, T. L.; Segall, B. Temperature-dependent exciton linewidths in semiconductors. *Phys. Rev. B* **1990**, *42*, 11218−11231.
(41) Hansen, K. R.; McClure, C. E.; Powell, D.; Hsieh, H.-C.; Flannery, L.; Garden, K.; Miller, E. J.; King, D. J.; Sainio, S.; Nordlund, D.; Colton, J. S.; Whittaker-Brooks, L. Low Exciton Binding Energies and Localized Exciton−Polaron States in 2D Tin Halide Perovskites. *Advanced Optical Materials* **2022**, *10*, No. 2102698.
(42) Wright, A. D.; Verdi, C.; Milot, R. L.; Eperon, G. E.; Pérez-Osorio, M. A.; Snaith, H. J.; Giustino, F.; Johnston, M. B.; Herz, L. M. Electron−phonon coupling in hybrid lead halide perovskites. *Nat. Commun.* **2016**, *7*, No. 11755.
(43) Lee, J.; Koteles, E. S.; Vassell, M. O. Luminescence linewidths of excitons in GaAs quantum wells below 150 K. *Phys. Rev. B* **1986**, *33*, 5512−5516.
(44) Gauthron, K.; Lauret, J. S.; Doyennette, L.; Lanty, G.; Al Choueiry, A.; Zhang, S. J.; Brehier, A.; Largeau, L.; Mauguin, O.; Bloch, J.; Deleporte, E. Optical spectroscopy of two-dimensional layered (C6H5C2H4-NH3)2-PbI4 perovskite. *Opt. Express* **2010**, *18*, 5912−5919.
(45) Urban, J. M.; Chehade, G.; Dyksik, M.; Menahem, M.; Surrente, A.; Trippe-Allard, G.; Maude, D. K.; Garrot, D.; Yaffe, O.; Deleporte, E.; Plochocka, P.; Baranowski, M. Revealing Excitonic Phonon Coupling in (PEA)2(MA)n-1PbnI3n+1 2D Layered Perovskites. *J. Phys. Chem. Lett.* **2020**, *11*, 5830−5835.
(46) Mitzi, D. B. Synthesis, Structure, and Properties of Organic-Inorganic Perovskites and Related Materials. *Prog. Inorg. Chem.* **1999**, *48*, 1−121.
(47) Saparov, B.; Mitzi, D. B. Organic-Inorganic Perovskites: Structural Versatility for Functional Materials Design. *Chem. Rev.* **2016**, *116*, 4558−96.

https://doi.org/10.1021/acs.nanolett.3c04895
Nano Lett. 2024, 24, 3638−3646

(48) Akselrod, G. M.; Deotare, P. B.; Thompson, N. J.; Lee, J.; Tisdale, W. A.; Baldo, M. A.; Menon, V. M.; Bulovic, V. Visualization of exciton transport in ordered and disordered molecular solids. *Nat. Commun.* **2014**, *5*, 3646.
(49) Li, W.; Huang, M. S. R.; Yadavalli, S. K.; Lizarazo Ferro, J. D.; Zhou, Y.; Zaslavsky, A.; Padture, N. P.; Zia, R. Direct Characterization of Carrier Diffusion in Halide-Perovskite Thin Films Using Transient Photoluminescence Imaging. *ACS Photonics* **2019**, *6*, 2375−2380.
(50) Saidaminov, M. I.; Williams, K.; Wei, M.; Johnston, A.; Quintero-Bermudez, R.; Vafaie, M.; Pina, J. M.; Proppe, A. H.; Hou, Y.; Walters, G.; Kelley, S. O.; Tisdale, W. A.; Sargent, E. H. Multi-cation perovskites prevent carrier reflection from grain surfaces. *Nat. Mater.* **2020**, *19*, 412−418.
(51) Andreani, L. C.; Tassone, F.; Bassani, F. Radiative lifetime of free excitons in quantum wells. *Solid State Commun.* **1991**, *77*, 641−645.
(52) Baldwin, A.; Delport, G.; Leng, K.; Chahbazian, R.; Galkowski, K.; Loh, K. P.; Stranks, S. D. Local Energy Landscape Drives Long-Range Exciton Diffusion in Two-Dimensional Halide Perovskite Semiconductors. *J. Phys. Chem. Lett.* **2021**, *12*, 4003−4011.
(53) Ovchinnikov, D.; Allain, A.; Huang, Y.-S.; Dumcenco, D.; Kis, A. Electrical Transport Properties of Single-Layer WS2. *ACS Nano* **2014**, *8*, 8174−8181.
(54) Jin, Z.; Li, X.; Mullen, J. T.; Kim, K. W. Intrinsic transport properties of electrons and holes in monolayer transition-metal dichalcogenides. *Phys. Rev. B* **2014**, *90*, 045422.
(55) Fivaz, R.; Mooser, E. Mobility of Charge Carriers in Semiconducting Layer Structures. *Phys. Rev.* **1967**, *163*, 743−755.
(56) Liang, A.; Gao, Y.; Asadpour, R.; Wei, Z.; Finkenauer, B. P.; Jin, L.; Yang, J.; Wang, K.; Chen, K.; Liao, P.; Zhu, C.; Huang, L.; Boudouris, B. W.; Alam, M. A.; Dou, L. Ligand-Driven Grain Engineering of High Mobility Two-Dimensional Perovskite Thin-Film Transistors. *J. Am. Chem. Soc.* **2021**, *143*, 15215−15223.
(57) Zhou, J.-J.; Hellman, O.; Bernardi, M. Electron-Phonon Scattering in the Presence of Soft Modes and Electron Mobility in SrTiO3 Perovskite from First Principles. *Phys. Rev. Lett.* **2018**, *121*, No. 226603.
(58) Xi, J.; Zheng, L.; Wang, S.; Yang, J.; Zhang, W. Temperature-dependent structural fluctuation and its effect on the electronic structure and charge transport in hybrid perovskite CH3NH3PbI3. *J. Comput. Chem.* **2021**, *42*, 2213−2220.

https://doi.org/10.1021/acs.nanolett.3c04895
Nano Lett. 2024, 24, 3638−3646